Research Article Vol. 12, No. 4 / April 2024 / Photonics Research 663

PHOTONICS Research

Frequency-comb-linearized, widely tunable lasers for coherent ranging

Baoqi Shi,[1,2,†] Yi-Han Luo,[2,3,†] Wei Sun,[2] Yue Hu,[2,3] Jinbao Long,[2] Xue Bai,[2] Anting Wang,[1,5] and Junqiu Liu[2,4,*]

[1]Department of Optics and Optical Engineering, University of Science and Technology of China, Hefei 230026, China
[2]International Quantum Academy, Shenzhen 518048, China
[3]Shenzhen Institute for Quantum Science and Engineering, Southern University of Science and Technology, Shenzhen 518055, China
[4]Hefei National Laboratory, University of Science and Technology of China, Hefei 230088, China
[5]e-mail: atwang@ustc.edu.cn
[†]These authors contributed equally to this work.
*Corresponding author: liujq@iqasz.cn

Received 31 October 2023; revised 26 January 2024; accepted 29 January 2024; posted 30 January 2024 (Doc. ID 510795); published 18 March 2024

Tunable lasers, with the ability to continuously vary their emission wavelengths, have found widespread applications across various fields such as biomedical imaging, coherent ranging, optical communications, and spectroscopy. In these applications, a wide chirp range is advantageous for large spectral coverage and high frequency resolution. Besides, the frequency accuracy and precision also depend critically on the chirp linearity of the laser. While extensive efforts have been made on the development of many kinds of frequency-agile, widely tunable, narrow-linewidth lasers, wideband yet precise methods to characterize and linearize laser chirp dynamics are also demanded. Here we present an approach to characterize laser chirp dynamics using an optical frequency comb. The instantaneous laser frequency is tracked over terahertz bandwidth at 1 MHz intervals. Using this approach we calibrate the chirp performance of 12 tunable lasers from Toptica, Santec, New Focus, EXFO, and NKT that are commonly used in fiber optics and integrated photonics. In addition, with acquired knowledge of laser chirp dynamics, we demonstrate a simple frequency-linearization scheme that enables coherent ranging without any optical or electronic linearization unit. Our approach not only presents novel wideband, high-resolution laser spectroscopy, but is also critical for sensing applications with ever-increasing requirements on performance. © 2024 Chinese Laser Press

https://doi.org/10.1364/PRJ.510795

1. INTRODUCTION

Tunable lasers, which have the ability to dynamically adjust their emission wavelength, have found widespread applications in a variety of industrial and scientific fields. For example, as shown in Fig. 1(a), in biomedical imaging, optical coherence tomography (OCT) [1–3] employs a widely tunable laser that provides a noninvasive and noncontact imaging modality for high-resolution, two-dimensional cross-sectional and three-dimensional volumetric imaging of tissue structures. In optical communication systems, optical frequency-domain reflectometry (OFDR) [4,5] uses tunable lasers for broadband loss and dispersion characterization. In laser spectroscopy, tunable diode laser absorption spectroscopy (TDLAS) [6–8] allows compound analysis of gases, as well as their conditions such as concentration, pressure, temperature, and velocity. For light detection and ranging (LiDAR), frequency-modulated continuous-wave (FMCW) LiDAR [9–14] uses a tunable laser to measure the distance (based on the time of flight) and speed (based on the Doppler effect) of a moving object.

In all of these applications, as well as others, the laser chirp range determines the measurement resolution and spectral bandwidth. However, due to the nonlinearity of laser gain and dynamics, tunable lasers typically exhibit chirping nonlinearity that is particularly deteriorated for a wide chirp range, as illustrated in Fig. 1(b). As a result, the laser chirp rate deviates from the set value, which compromises the frequency resolution, precision, and accuracy in applications. Therefore, widely tunable lasers require careful characterization and linearization for demanding applications.

To track the laser chirp rate, a fiber unbalanced Mach–Zehnder interferometer (UMZI) is commonly used to calibrate the instantaneous laser frequency, e.g., in data processing [15–17], active linearization [9], and laser drive signal optimization [18]. However, for a wide chirp range, the fiber

dispersion seriously reduces the calibration precision of fiber UMZIs and causes phase-instability issues, leading to insufficient accuracy for linearization. In comparison, fully stabilized optical frequency combs (OFCs) with equidistant grids of frequency lines can essentially resolve these issues [10,19–22].

Here we demonstrate an approach to characterize the chirp dynamics of widely tunable lasers. We apply this method on 12 lasers from Toptica, Santec, New Focus, EXFO, and NKT that are commonly used in fiber optics and integrated photonics. Using an OFC and digital band-pass filters, the instantaneous laser frequency is tracked with 1 MHz intervals over terahertz bandwidth. This allows the linearization of laser frequency with pre-calibrated chirp rate, particularly useful for coherent LiDAR.

2. PRINCIPLE AND SETUP

To measure the laser chirp rate, we use a commercial, fully stabilized, fiber-based OFC (Quantum CTek) as a frequency "ruler" [23–25] to trace the instantaneous laser frequency during chirping. In our case, the comb repetition rate $f_{\mathrm{rep}} = 200$ MHz and its carrier envelope offset frequency f_{ceo} are actively locked to a rubidium atomic clock; thus the OFC is fully stabilized. Consequently, in the frequency domain, the nth comb line's frequency is unambiguously determined as $f_n = f_{\mathrm{ceo}} + n \cdot f_{\mathrm{rep}}$ $(n \in \mathbb{N})$.

When the laser chirps, it beats against tens of thousands of comb lines with precisely known frequency values, as shown in Fig. 2(a). Beat signals of frequencies $|f_n - f_l(t)|$ are generated, where $f_l(t)$ is the instantaneous frequency of the tunable laser at time t. As the frequency comb is fully stabilized, for a mode-hop-free tunable laser, the dynamics and linearity of $f_l(t)$ are projected onto the beat signals. The simplest beat signals to analyze are the two generated by the tunable laser with its two neighboring comb lines, i.e., $|f_n - f_l(t)| < f_{\mathrm{rep}} = 200$ MHz. Experimentally, the two beat signals are recorded by an oscilloscope after passing through a low-pass filter (LPF, Mini-Circuits, BLP–150+), whose 3-dB cutoff frequency is 155 MHz in our case. We denote the frequencies of the two beat signals as β_1 and β_2 $(\beta_1 + \beta_2 = f_{\mathrm{rep}} = 200$ MHz and $\beta_1 < \beta_2)$. As shown in Fig. 2(b), for a continuous linear chirp, when the laser frequency passes through the comb lines sequentially, β_1 and β_2 vary in a sawtooth waveform. The time-domain waveform near $\beta_1 = 0$ is shown in the leftmost panel of Fig. 2(d), corresponding to the situation when the laser chirps across a comb line.

Here, we concentrate on the analysis of β_1, since $\beta_1 + \beta_2 = 200$ MHz. The dynamics and linearity of $\beta_1(t)$ as a function of time are identical to those of the laser frequency $f_l(t)$. We process the $\beta_1(t)$ signal and extract the instantaneous frequency value as illustrated in Fig. 2(d). A finite impulse response (FIR) band-pass filter with a specific pass-band center frequency f_{FIR} is applied to the recorded $\beta_1(t)$ signal. The FIR filter only transmits the temporal segments when $\beta_1(t)$ is around f_{FIR}, as illustrated in the left middle panel of Fig. 2(d). Then Hilbert transform [26] is applied to obtain the pulse's envelope. Via peak searching, the exact time of the pulses' centers is extracted and recorded when $\beta_1(t) = f_{\mathrm{FIR}}$. Experimentally, we repeatedly apply FIR filters whose f_{FIR} values are digitally set from 3 to 97 MHz with an interval of $\Delta f_{\mathrm{FIR}} = 1$ MHz, as shown in Fig. 2(e). In this way, during

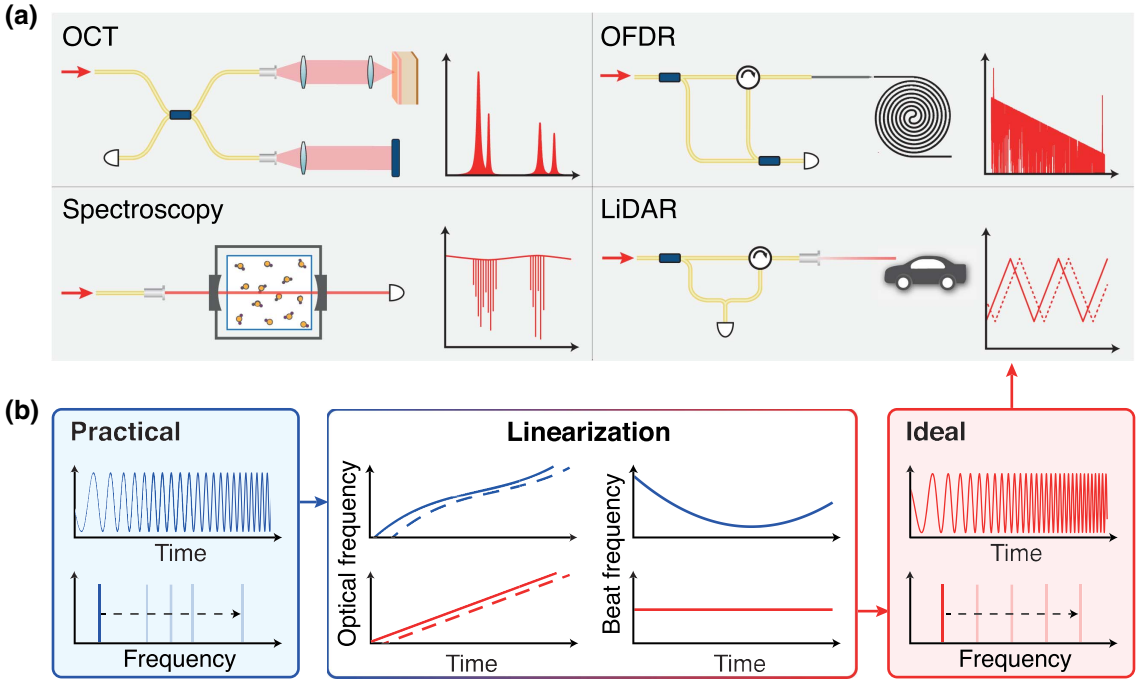

Fig. 1. Applications and principle of widely tunable lasers. (a) Applications requiring linearly chirping lasers. OCT, optical coherence tomography; OFDR, optical frequency-domain reflectometry; LiDAR, light detection and ranging. (b) Principle of laser chirp linearization. An ideal laser chirps at a constant rate. However, in reality, the actual chirp rate varies. By beating the laser with its delayed part, the chirp nonlinearity in the optical domain is revealed in the radio frequency (RF) domain.

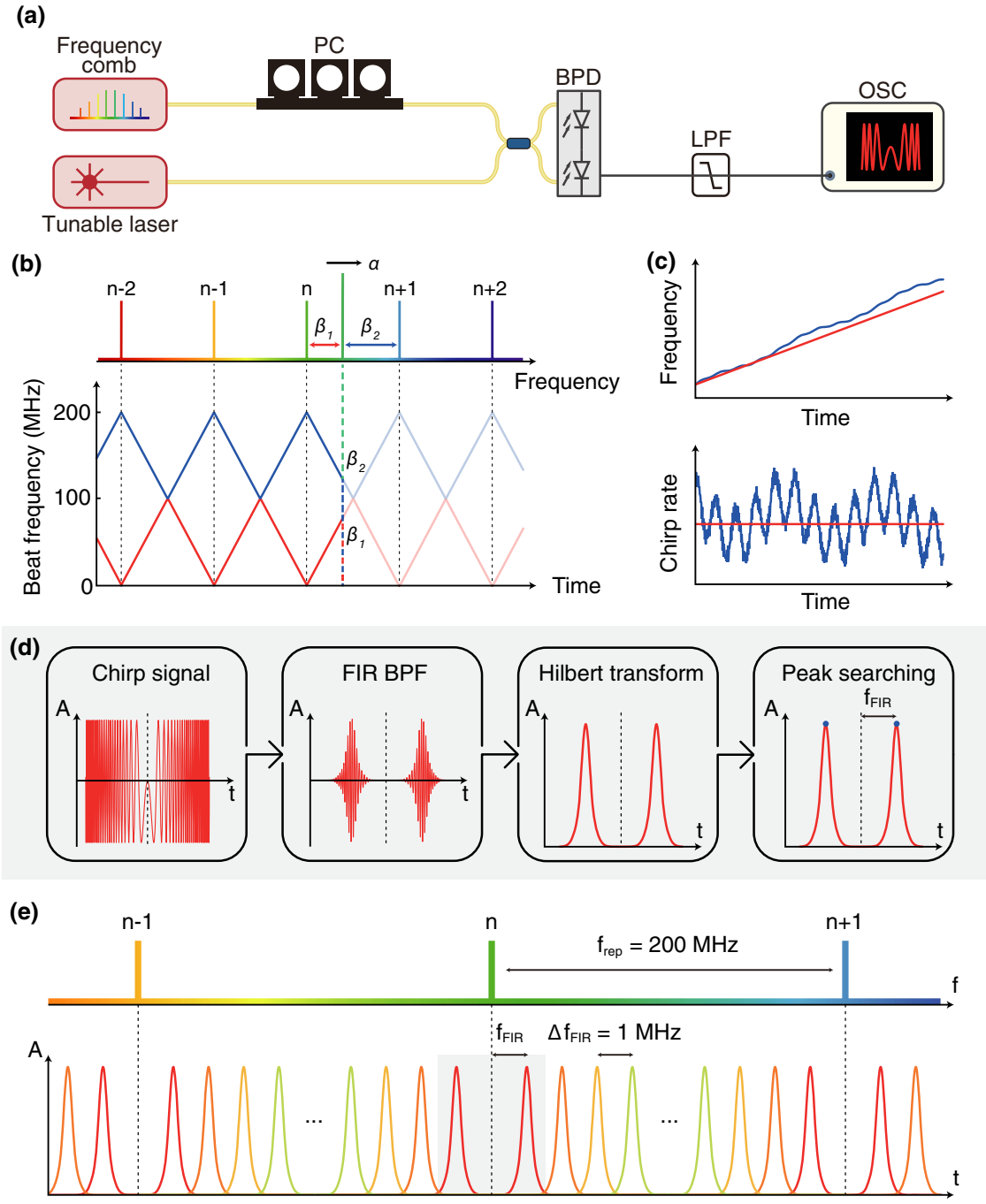

Fig. 2. Schematic and experimental setup of laser chirp characterization. (a) Experimental setup. BPF, band-pass filter; PC, polarization controller; BPD, balanced photodetector; LPF, low-pass filter; OSC, oscilloscope. (b) Illustration of the laser frequency beating with the OFC during laser chirping at a rate of α. The time traces of the two beat frequencies β_1 and β_2 ($\beta_2 > \beta_1$) are shown. (c) Upper panel shows the instantaneous frequency of the tunable laser in the ideal (red) and actual (blue) cases. Lower panel shows the corresponding instantaneous chirp rate α. (d) Flowcharts of the algorithm based on finite impulse response (FIR) band-pass filters (BPFs), to extract the instantaneous laser frequency as well as the chirp rate. The dashed lines mark the time where the laser frequency scans across a comb line. (e) The FIR filter's center frequency f_{FIR} is digitally set, and the instantaneous laser frequency is calculated over 1 MHz intervals.

continuous laser chirp over a wide bandwidth, the $\beta_1(t)$ time trace is frequency-calibrated and recorded with 1 MHz intervals.

Next, we unwrap the sawtooth-like $\beta_1(t)$ trace. Pulses corresponding to $f_{\mathrm{FIR}} = 3$ MHz are selected as markers. As shown in the bottom panel of Fig. 2(e), when the laser chirps over a pair of comb lines (dashed lines), i.e., f_{rep} distance, two markers are created by the $f_{\mathrm{FIR}} = 3$ MHz filters. With the known comb spacing $f_{\mathrm{rep}} = 200$ MHz, $\beta_1(t)$ can then be unwrapped to an increasing function of time t, which is

$\Delta f(t) = f_l(t) - f_l(t_0)$, where $f_l(t_0)$ is the starting laser frequency at time t_0. As shown in Fig. 2(c), the instantaneous chirp rate—estimated as the average rate within $\Delta f_{\mathrm{FIR}} =$ 1 MHz calibration interval—is calculated as $\alpha(t) = \mathrm{d}\Delta f(t)/\mathrm{d}t$, and is later used for chirp linearization.

3. RESULTS

A. Laser Chirp Dynamics Characterization

Now we use this frequency-comb-calibrated method to characterize a total of 10 widely tunable, mode-hop-free, external-cavity diode lasers (ECDLs), including three Toptica CTL lasers, four Santec lasers, two New Focus lasers, and one EXFO laser. These lasers are all operated in the telecommunication band around 1550 nm, and are extensively used in fiber optics and integrated photonics. For example, Toptica CTL and New Focus lasers are widely used in the generation of microresonator-based dissipative Kerr soliton frequency combs [27–35]. Santec and EXFO lasers are widely used in the wideband characterization of waveguide dispersion [6,22,33,36,37]. In addition, two NKT fiber lasers are characterized, although their frequency tuning ranges are significantly narrower.

An ECDL typically has two tuning modes, i.e., the wide and fine tuning modes. In the wide tuning mode, the external cavity length that determines the laser frequency is controlled by a stepper motor, enabling a frequency tuning range exceeding 10 THz. In the fine tuning mode, the external cavity length is controlled by a piezo under an external voltage that determines the laser frequency. In this mode, the laser can only be tuned by tens of gigahertz. Triangular and sinusoidal voltage signals are often used to drive the piezo, and to determine the laser chirp range B and modulation frequency f_{mod}. The average chirp rate is $\overline{\alpha_{\mathrm{set}}} = 2Bf_{\mathrm{mod}}$.

First, we characterize these lasers in the wide tuning mode. We take one Toptica CTL laser as the first example. Experimentally, the laser is configured to a single run that chirps from 1550 to 1560 nm. On the laser panel, we manually set the chirp rate α_{set} to 1, 2, 5, and 10 nm/s. Experimentally, we characterize the Toptica laser's output power variation, which is below 1% over 10 MHz spectral width. Since the FIR filter's 3-dB pass bandwidth is smaller than 10 MHz, this laser power variation is too small to change the SNR of the beatnote.

The oscilloscope's sampling resolution is set to 155 Hz for different α_{set}. The instantaneous chirp rate $\alpha(t)$ within 1 MHz intervals is tracked, allowing retrieval of the instantaneous laser frequency $f_l(t)$ as well as the wavelength $\lambda(t)$. In this manner, $\alpha(t)$ can be converted to $\alpha(\lambda)$ for a better comparison among cases of different α_{set} in the same scale.

Figure 3 shows representative $\alpha(\lambda)$ traces with different α_{set} within a 0.2 nm wavelength range (1555–1555.2 nm) during chirping. To facilitate comparison, we normalize the measured $\alpha(\lambda)$ to the set value α_{set} on the laser panel; i.e., the normalized chirp rate is $\alpha(\lambda)/\alpha_{\mathrm{set}}$. Here $\alpha(\lambda)/\alpha_{\mathrm{set}} = 1$ corresponds to a perfectly linear chirp at a constant rate. Figure 3(a) shows that the experimentally measured $\alpha(\lambda)/\alpha_{\mathrm{set}}$ fluctuates and exhibits nonlinearity. Particularly, when $\alpha_{\mathrm{set}} = 1$ and 5 nm/s, prominent frequency oscillation is observed; whereas for $\alpha_{\mathrm{set}} = 2$ and 10 nm/s, this oscillation is inhibited. The oscillation pattern of $\alpha(\lambda)/\alpha_{\mathrm{set}}$ is repeated every 1.6 pm, probably due to the laser's intrinsic configuration or regulation. Besides, mechanical modes of the external laser cavity might also cause chirp rate jitter. Figure 3(b) shows $\alpha(t)/\alpha_{\mathrm{set}}$ spectra in the frequency domain. The amplitude of the spectra presents the chirp rate jitter strength. A component at 3.84 kHz Fourier offset frequency—independent of α_{set}—is revealed, likely linking to the eigen-frequency of the cavity's fundamental mechanical mode. Higher-order mechanical modes can also be observed in Fig. 3(b) at 28.22 kHz and 56.43 kHz frequencies when the laser chirps more slowly.

Since Fig. 3(a) shows the optimal laser chirping performance at $\alpha_{\mathrm{set}} = 2$ and 10 nm/s, we further investigate $\alpha(\lambda)/\alpha_{\mathrm{set}}$ over the entire 10 nm bandwidth. Figure 3(c) shows the laser's chirp rate drift with $\alpha_{\mathrm{set}} = 2$ and 10 nm/s. Limited by the oscilloscope's memory depth (400 Mpts) and sampling rate (400 MSa/s), we can only acquire data in 1 s. We set the laser to repeatedly chirp from 1550 to 1560 nm, and characterize one segment of the chirp trace each time. Multiple segments displayed with different colors are stitched to form a complete trace covering the full 10 nm range. It becomes apparent that, although Fig. 3(c) bottom shows weak chirp rate jitter with $\alpha_{\mathrm{set}} = 10$ nm/s, the overall chirp rate drifts considerably. With $\alpha_{\mathrm{set}} = 2$ nm/s, the laser completes its acceleration at 1550.5 nm and reaches stability at 1552.0 nm, until it begins to decelerate at 1559.5 nm. The laser maintains good linearity in the center 7.5 nm range. We therefore conclude that, in the wide tuning mode, the optimal chirp rate of Toptica CTL is $\alpha_{\mathrm{set}} = 2$ nm/s.

We further characterized another two Toptica CTL lasers, four Santec lasers, two New Focus lasers, and one EXFO laser in their wide tuning modes. The laser chirping performance is investigated within 1550–1560 nm bandwidth, and α_{set} is set from 1 to 200 nm/s. Table 1 presents a summary of different lasers' chirp dynamics with their respective optimal α_{set}. We refer the readers to Appendix A for detailed characterization results of each laser, which can be useful for readers currently using these lasers. Overall, in the wide tuning mode, the Santec and EXFO lasers work best with $\alpha_{\mathrm{set}} = 100$ nm/s, and the Toptica CTL and New Focus lasers work best with $\alpha_{\mathrm{set}} = 2$ nm/s.

To show the deviation of laser chirp rate from $\alpha(t)/\alpha_{\mathrm{set}} = 1$, we calculate the root mean square error (RMSE) as

$$\mathrm{RMSE} = \sqrt{\frac{\sum_{i=1}^{T} (\alpha_i/\alpha_{\mathrm{set}} - 1)^2}{T}}, \tag{1}$$

where α_i is the sample of the chirp rate and T is the sample number. Besides, the wavelength linearity can be estimated by nonlinearity error [38] $\delta_L = \Delta\lambda_{\mathrm{max}}/\lambda_{\mathrm{f.s.}}$, where $\Delta\lambda_{\mathrm{max}}$ is the maximum deviation of the measured wavelength from its linearly fitted value, and $\lambda_{\mathrm{f.s.}}$ is the full-scale wavelength range. This indicator mainly considers whether the laser chirp is linear, but not whether the average chirp rate $\overline{\alpha_{\mathrm{set}}}$ matches the set value α_{set}. Particularly, Table 1 shows that the EXFO laser features the smallest RMSE and δ_L with $\alpha_{\mathrm{set}} = 100$ nm/s.

Next, we characterized 11 lasers in the fine tuning modes, including three Toptica CTL lasers, four Santec lasers, two

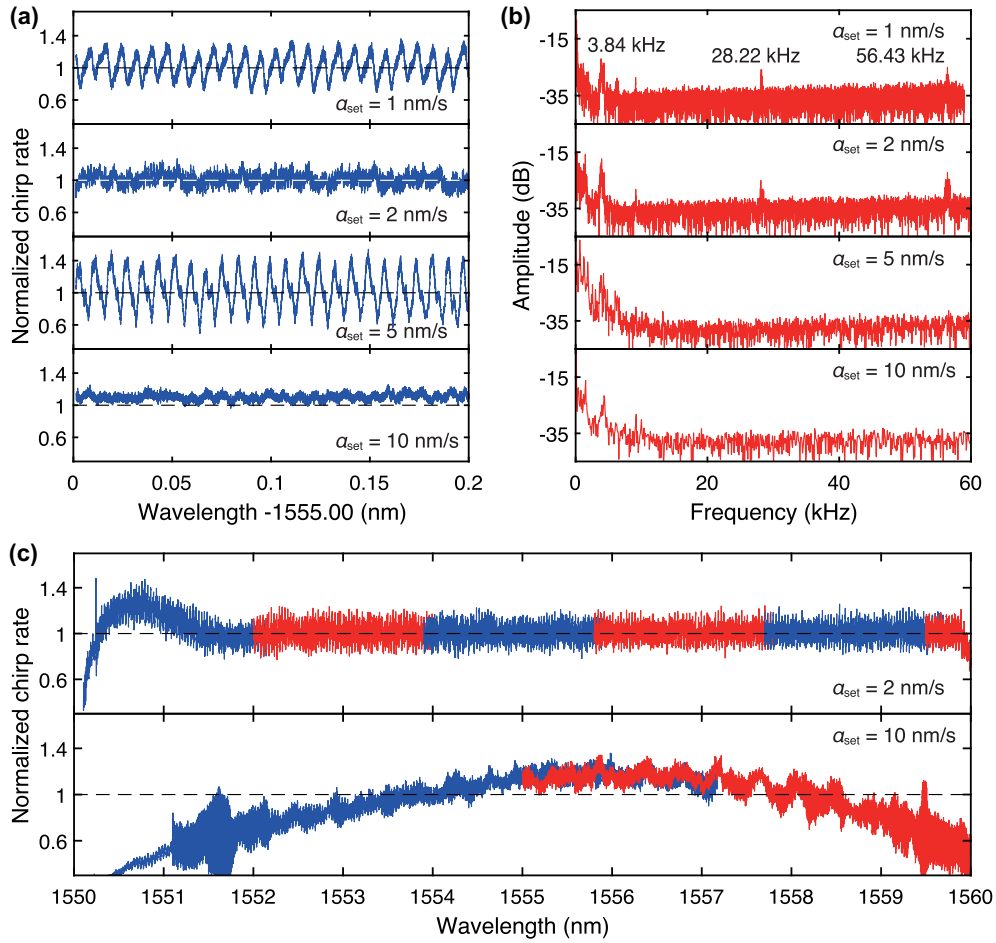

Fig. 3. Characterization of Toptica CTL laser's chirp dynamics. (a) Normalized chirp rate $\alpha(\lambda)/\alpha_{set}$ with different set values α_{set} over 0.2 nm wavelength range. (b) Frequency spectra of the normalized chirp rate $\alpha(t)/\alpha_{set}$. The frequency values of prominent peaks are marked. (c) Normalized chirp rate $\alpha(\lambda)/\alpha_{set}$ with different set values α_{set} over 10 nm wavelength range.

New Focus lasers, and two NKT lasers. We note that the EXFO laser does not feature the fine tuning mode. These lasers are frequency-modulated at 193.3 THz optical frequency and with an excursion range of 10 GHz (except 8 GHz for the NKT lasers). The drive voltage signal to the piezo is either triangular or sinusoidal. We set the modulation frequency f_{mod} to 2, 10, 50, and 100 Hz. For normalization, the set chirp rate $\alpha_{set}(t)$ is calculated according to the drive signal. The optimal f_{mod} for different lasers with different drive manners is listed in Table 1 (see Appendix B for detailed characterization results of each laser). For the cases with sinusoidal drive, α_{set} represents the average set chirp rate $\overline{\alpha_{set}}$. For the Toptica CTL and New Focus

Table 1. Comparison of Laser Chirp Dynamics of Different Lasers with Different Conditions

Laser Brand	Model	Tuning Mode	Optimal α_{set}	f_{mod}	Chirp Range	RMSE	δ_L
Toptica	CTL 1550	Wide, single	2 nm/s (0.24 THz/s)	–	10 nm (1.2 THz)	7.5% (1.1%)	0.2% (0.0%)
Santec	TSL-570-A	Wide, single	100 nm/s (12 THz/s)	–	10 nm (1.2 THz)	6.8% (1.6%)	0.4% (0.2%)
New Focus	TLB-6700	Wide, single	2 nm/s (0.24 THz/s)	–	10 nm (1.2 THz)	12.9% (1.9%)	0.3% (0.2%)
EXFO	T500S	Wide, single	100 nm/s (12 THz/s)	–	10 nm (1.2 THz)	4.8%	0.2%
Toptica	CTL 1550	Fine, triangular	1.6 nm/s (200 GHz/s)	10 Hz	80 pm (10 GHz)	7.8% (1.3%)	0.8% (0.0%)
Santec	TSL-570-A	Fine, triangular	1.6 nm/s (200 GHz/s)	10 Hz	80 pm (10 GHz)	14.1% (0.6%)	1.8% (0.1%)
New Focus	TLB-6700	Fine, triangular	8 nm/s (1 THz/s)	50 Hz	80 pm (10 GHz)	17.9% (12.1%)	0.4% (0.1%)
NKT	E15	Fine, triangular	256 pm/s (32 GHz/s)	2 Hz	64 pm (8 GHz)	5.6% (1.9%)	0.5% (0.3%)
Toptica	CTL 1550	Fine, sinusoidal	8 nm/s (1 THz/s)	50 Hz	80 pm (10 GHz)	7.4% (0.2%)	–
Santec	TSL-570-A	Fine, sinusoidal	1.6 nm/s (200 GHz/s)	10 Hz	80 pm (10 GHz)	16.4% (0.5%)	–
New Focus	TLB-6700	Fine, sinusoidal	16 nm/s (2 THz/s)	100 Hz	80 pm (10 GHz)	8.4% (4.2%)	–
NKT	E15	Fine, sinusoidal	256 pm/s (32 GHz/s)	2 Hz	64 pm (8 GHz)	6.5% (1.0%)	–

lasers, different drives have different effects, as the triangular drive may cause resonance in the piezo at certain frequencies (see Appendix B). Therefore, these lasers behave better with a sinusoidal drive.

B. Light Detection and Ranging

Based on our frequency-comb-calibrated laser chirp dynamics, we further demonstrate a linearization method for widely tunable lasers for FMCW LiDAR. LiDAR can quickly and accurately map the environment, provide insights into the structure and composition, and allow operators to make informed decisions on the protection of natural resources [39,40] and environment [41,42] or manage agriculture [43]. For autonomous vehicles, LiDAR enables safe and reliable navigation by providing high-resolution, real-time 3D mapping of the environment [44–47]. The technology has also revolutionized archaeology, allowing nondestructive imaging of hidden features and artifacts [48–50].

The principle of LiDAR is to project an optical signal onto a moving object. The reflected or scattered signal is received and processed to determine the object's distance from the laser [13,51]. The light received by the photodetector experiences a time delay τ from its emission time. Thus the object's distance is calculated as $d = c\tau/2$, where c is the speed of light. For FMCW LiDAR, the time delay τ is obtained in a coherent way [9,10,14]. The frequency-modulated laser is split into two paths as shown in the LiDAR panel of Fig. 1(a). In one path, the laser passes through a collimator, enters free space, and is reflected by the object. The reflected laser is then combined with the reference path, and the beat signal between the two paths is recorded by a photodetector. If the laser frequency is modulated linearly at a constant chirp rate α, the time delay τ creates a beat signal of frequency $\Delta f = \alpha\tau$. Thus, the photodetected beat signal is

$$V(t) \propto \cos(2\pi\Delta f t) = \cos\left(2\pi\alpha\frac{2d}{c}t\right). \tag{2}$$

Equation (2) indicates that the distance d can be obtained with fast Fourier transformation on t.

The ranging resolution [15] δd of FMCW LiDAR is limited by the chirp range B, as $\delta d = c/2B$. High resolution, i.e., small δd, requires a large B of the tunable laser. However, chirp nonlinearity causes a varying α over time. Consequently, the beat frequency Δf varies as shown in Fig. 1(b). To extract the precise value of d from $V(t)$, an accurate trace of $\alpha(t)$ is mandatory, necessitating the calibration of the instantaneous laser frequency during chirping. The chirp linearization is performed by rescaling the beat signal's time axis by $t' = \alpha(t)t$ to

$$V(t') = \cos\left(2\pi\frac{2d}{c}t'\right). \tag{3}$$

Here, using our frequency-comb-calibration method, the characterized laser chirp rate $\alpha(t)$ in return allows chirp rate linearization. The chirp rate can be pre-linearized when the laser is tuned by a piezo, i.e., when the laser is working in the fine tuning mode. Again we use the Toptica CTL laser as the example. The laser has optimal performance of chirp linearity when driven by a 50 Hz sinusoidal wave. The chirp range is set to 35 GHz in the fine tuning mode, and $\alpha(t)$ is characterized (see Appendix C). The same characterization of $\alpha(t)$ is performed three times, and the averaged result is used as the pre-linearized chirp rate $\alpha_c(t)$. By rescaling the time axis in Eq. (2) by $t' = \alpha_c(t)t$, the laser is pre-linearized and the range profile can be extracted from Eq. (3). The photodetected signal is rescaled with t'. Zero-padding [52] is also implemented to reduce resolution ambiguities. We note that the pre-linearization does not function well for the stepper motor-based wide tuning mode.

Finally, we proceed with a LiDAR experiment without any linearization unit (see Appendix D). Experimentally, a stainless steel cylinder with an engraved text of 2.8 mm depth on its surface is imaged using our LiDAR setup. The stainless steel cylinder is placed on a 2D translation stage 4 m away from the collimator. As the translation stage moves, the distance between the cylinder surface and the collimator is continuously measured to produce a 2D ranging map.

To highlight the effect of linearization, we measure the surface profile using two methods, i.e., with pre-linearization and without any linearization. We emphasize that the former case only requires a characterized $\alpha_c(t)$ as prior knowledge for signal processing; neither OFC nor real-time frequency calibration is used in the ranging experiment. To retrieve the ranging profile, for pre-linearization, the beat signal $V(t')$ of Eq. (3) is rewritten as $V(l') = \cos(2\pi d l')$, where $l' = 2t'/c$. By fast Fourier transform on l', the space spectrum is obtained, as shown in the top panel of Fig. 4(b). The peak corresponds to the distance $d = 4$ m of the surface to the laser. For the case without linearization, the beat signal $V(t)$ of Eq. (2) is rewritten as $V(l) = \cos(2\pi d l)$, where $l = 2\alpha_{\text{set}}t/c$ and α_{set} is the set chirp rate. The space spectrum obtained by fast Fourier transform on l is shown in the bottom panel of Fig. 4(b). Without linearization, the peak is broadened due to ranging imprecision, leading to ambiguous determination of distance. Figure 4(a) shows the measured relative distance map with pre-linearization (left) and without any linearization (right). The long-term stability of pre-linearization is verified by a precision test (see Appendix D).

4. CONCLUSION

In conclusion, we have demonstrated an approach to characterize chirp dynamics of widely tunable lasers based on an OFC. Compared to the frequency calibration method using a UMZI, our method is more accurate and precise (see Appendix E for details). Using this method we have characterized 12 lasers including three Toptica CTL lasers, four Santec lasers, two New Focus lasers, two NKT fiber lasers, and one EXFO laser. By comparing the laser's chirp linearity with different settings, the optimal operation condition of each laser is found. For example, the optimal chirp rates of Toptica CTL, New Focus, Santec, and EXFO lasers are $\alpha_{\text{set}} = 2$, 2, 100, and 100 nm/s, respectively. Operating the laser with its optimal setting and pre-linearizing laser chirp, we successfully apply the laser for coherent LiDAR without any extra linearization unit. Field-programmable gate arrays (FPGAs) to implement multiple FIR filters can be further added to increase data processing speed and reduce the amount of data to be stored by real-time data processing. Our method of characterizing and

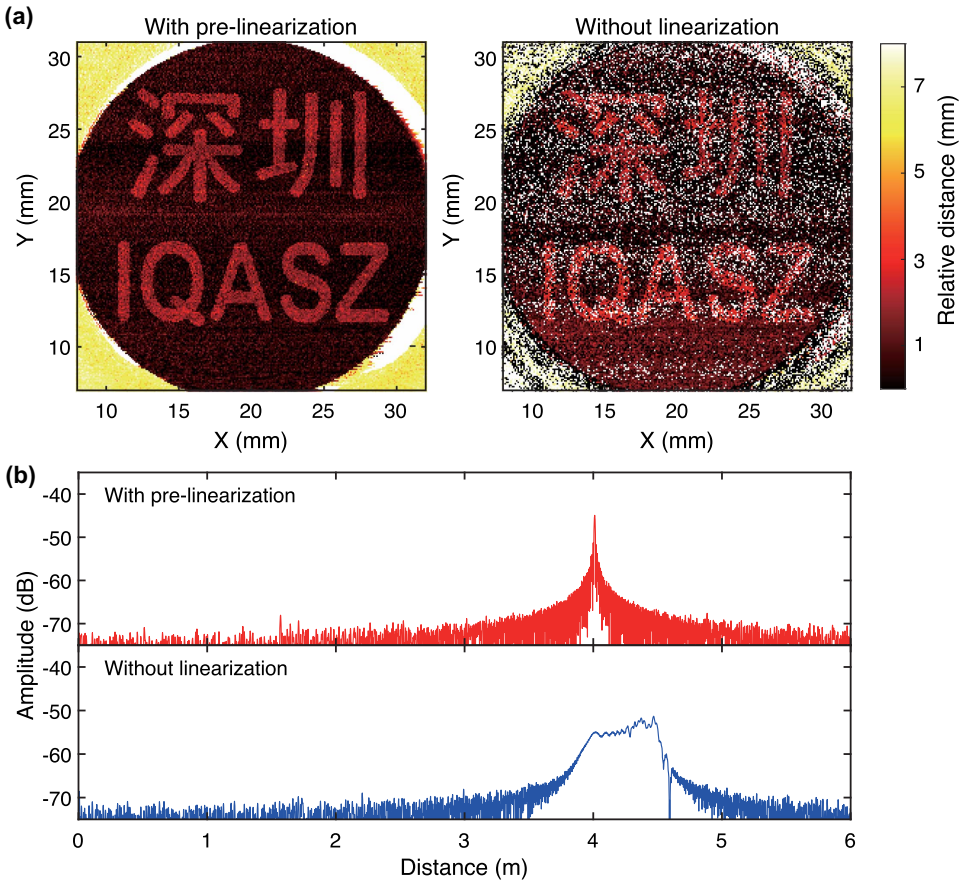

Fig. 4. Coherent LiDAR experiment. (a) Maps of measured relative distance of an engraved surface with pre-linearization and without linearization. The sample's tilt angle of 11.6° is measured and subtracted. (b) Space spectra of the ranging profiles obtained with pre-linearization and without linearization. Fast Fourier transform is applied on the ranging profile of each case to retrieve the spectrum. The peaks correspond to the distance $d = 4$ m of the surface to the laser.

pre-linearizing laser chirp dynamics has been proven to be a critical diagnostic method for applications such as OCT, OFDR, and TDLAS.

APPENDIX A: LASER CHIRP DYNAMICS IN THE WIDE TUNING MODE

For the wide tuning mode, we have characterized 10 lasers. These lasers include three Toptica CTL lasers, four Santec lasers, two New Focus lasers, and one EXFO laser. Experimentally, the lasers are configured to a single run that chirps from 1550 to 1560 nm. On the laser panel, we manually set the chirp rate α_{set} to 1, 2, 5, 10, 50, 100, and 200 nm/s. The oscilloscope's sampling resolution is set to 155 Hz for different α_{set}. The instantaneous chirp rate $\alpha(t)$ within 1 MHz interval is tracked, allowing retrieval of the instantaneous laser frequency $f_l(t)$ as well as the wavelength $\lambda(t)$. In this manner, $\alpha(t)$ can be converted to $\alpha(\lambda)$ for a better comparison between cases with different α_{set}. A summary of different lasers' chirp dynamics with different α_{set} is shown in Table 2.

The Toptica lasers support a maximum chirp rate of 10 nm/s. Besides the chirp dynamics of the Toptica laser as shown in Fig. 3, the comparison of three Toptica lasers is shown in Fig. 5. The 1.6-pm-oscillation pattern mentioned in the main text when $\alpha_{set} = 1$ nm/s exists in all three Toptica lasers as shown in Fig. 5(a). Meanwhile, for $\alpha_{set} = 2$ nm/s, this oscillation is inhibited. As shown in Fig. 5(b), the chirp rate jitter frequencies of 3.84, 28.22, and 56.43 kHz occur in all these Toptica lasers.

The Santec lasers support a maximum chirp rate of 200 nm/s. However, two Santec lasers exhibit mode hopping when $\alpha_{set} < 5$ nm/s, so the corresponding laser chirp dynamics of the Santec lasers are not shown. As shown in Fig. 6, when α_{set} is relatively small, the actual chirp rate has main jitter frequencies of 2.06, 16.04, 32.08, 64.10, 96.15, and 128.17 kHz. These jitter frequencies occur in all four Santec lasers, which is shown in Fig. 7, although their jitter amplitudes are different. These jitters become less pronounced as α_{set} increases. In Fig. 6(c), we show the normalized chirp rate over the full 10 nm chirp range for $\alpha_{set} = 100$ nm/s. The Santec laser performs well throughout the set chirp range, with no acceleration or deceleration in between. By comparing the laser chirp dynamics in Table 2, we conclude that, in the wide tuning mode, the optimal chirp rate of Santec lasers is $\alpha_{set} = 50$ and 100 nm/s.

Table 2. Comparison of Laser Chirp Dynamics of Different Lasers in the Wide Tuning Mode

Laser Brand	Model	Tuning Mode	Chirp Range	α_{set}	RMSE	δ_L
Toptica	CTL 1550	Wide, single	10 nm	1 nm/s	16.9% (2.4%)	0.2% (0.0%)
Toptica	CTL 1550	Wide, single	10 nm	2 nm/s	7.5% (1.1%)	0.2% (0.0%)
Toptica	CTL 1550	Wide, single	10 nm	5 nm/s	26.2% (3.4%)	0.5% (0.4%)
Toptica	CTL 1550	Wide, single	10 nm	10 nm/s	14.7% (3.3%)	0.3% (0.2%)
Santec	TSL-570-A	Wide, single	10 nm	5 nm/s	14.5% (6.0%)	0.5% (0.3%)
Santec	TSL-570-A	Wide, single	10 nm	10 nm/s	11.3% (3.9%)	0.7% (0.3%)
Santec	TSL-570-A	Wide, single	10 nm	20 nm/s	14.0% (6.3%)	1.4% (0.8%)
Santec	TSL-570-A	Wide, single	10 nm	50 nm/s	6.9% (1.8%)	0.4% (0.3%)
Santec	TSL-570-A	Wide, single	10 nm	100 nm/s	6.8% (1.6%)	0.4% (0.2%)
Santec	TSL-570-A	Wide, single	10 nm	200 nm/s	8.9% (1.6%)	0.3% (0.2%)
New Focus	TLB-6700	Wide, single	10 nm	1 nm/s	13.9% (1.1%)	0.4% (0.0%)
New Focus	TLB-6700	Wide, single	10 nm	2 nm/s	12.9% (1.9%)	0.3% (0.2%)
New Focus	TLB-6700	Wide, single	10 nm	5 nm/s	13.6% (1.4%)	0.8% (0.4%)
New Focus	TLB-6700	Wide, single	10 nm	10 nm/s	14.8% (4.0%)	0.9% (0.6%)
New Focus	TLB-6700	Wide, single	10 nm	20 nm/s	17.1% (3.4%)	0.6% (0.4%)
EXFO	T500S	Wide, single	10 nm	20 nm/s	15.1%	1.6%
EXFO	T500S	Wide, single	10 nm	50 nm/s	6.5%	0.5%
EXFO	T500S	Wide, single	10 nm	100 nm/s	4.8%	0.2%
EXFO	T500S	Wide, single	10 nm	200 nm/s	48.9%	0.2%

The New Focus lasers support a maximum chirp rate of 20 nm/s. As shown in Fig. 8, the New Focus laser behaves similarly at different α_{set}. The main jitter frequencies are 0.68, 2.62, and 8.43 kHz. The performance over the full chirp range in Fig. 8(c) shows that the laser is not stable at the maximum chirp rate of 20 nm/s. When the chirp rate is $\alpha_{set} = 10$ nm/s, the laser reaches stability at 1551.5 nm and keeps at a chirp rate of the set value. As shown in Table 2, the New Focus lasers have better linearity when $\alpha_{set} < 5$ nm/s.

The EXFO laser supports a maximum chirp rate of 200 nm/s but a minimum chirp rate of 20 nm/s. The jitter frequency is enormous at 8.21 kHz, while no other obvious jitter frequencies are observed, as shown in Fig. 9. When $\alpha_{set} =$ 200 nm/s, the laser does not finish the chirp rate acceleration

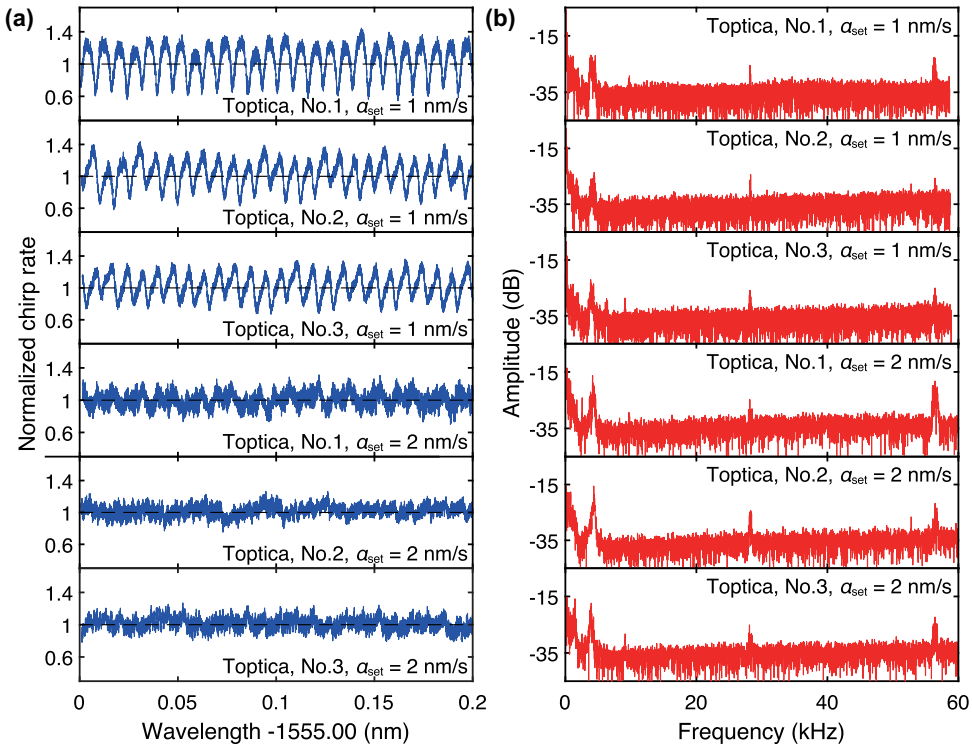

Fig. 5. Comparison of three Toptica lasers' chirp dynamics in the wide tuning mode. (a) Normalized chirp rate $\alpha(\lambda)/\alpha_{set}$ of the three Toptica lasers with different set values α_{set} over 0.2 nm wavelength range. (b) Frequency spectra of the chirp rate $\alpha(t)/\alpha_{set}$.

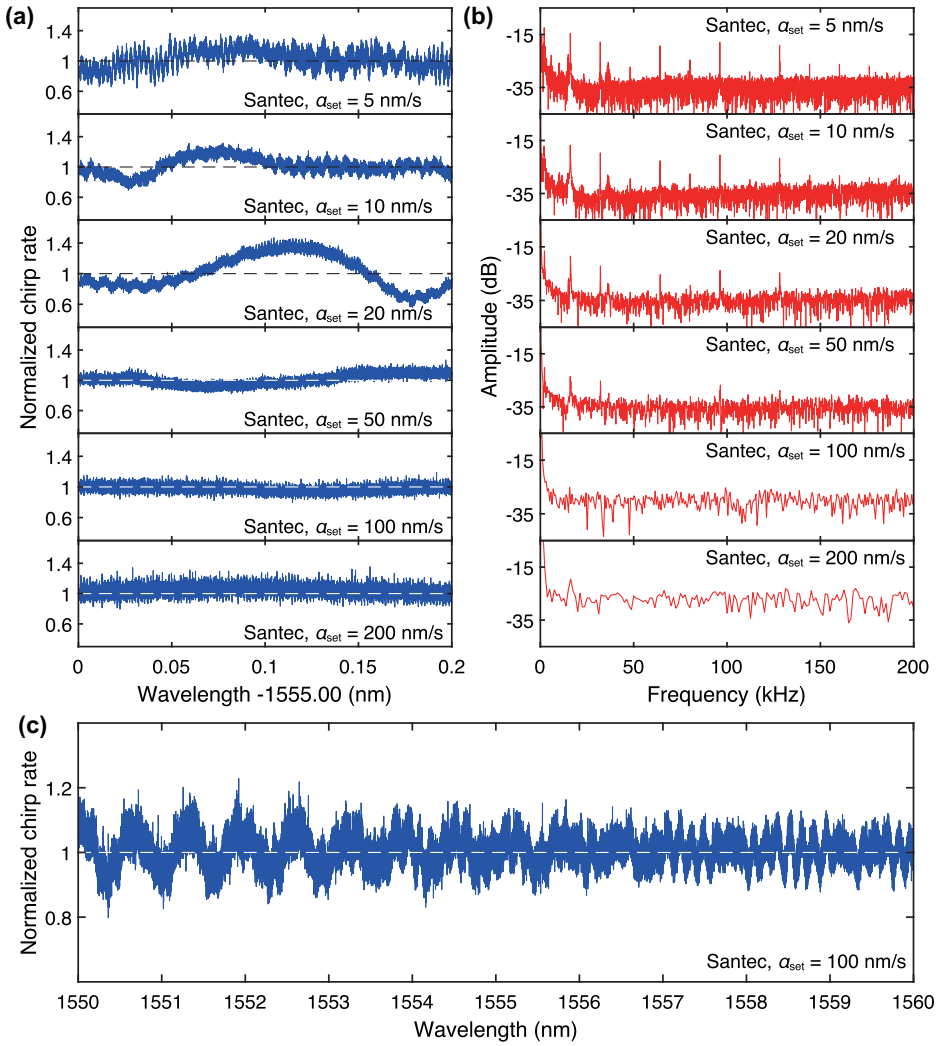

Fig. 6. Characterization of chirp dynamics of a Santec laser in the wide tuning mode. (a) Normalized chirp rate $\alpha(\lambda)/\alpha_{set}$ with different set values α_{set} over 0.2 nm wavelength range. (b) Frequency spectra of the chirp rate $\alpha(t)/\alpha_{set}$. (c) Normalized chirp rate $\alpha(\lambda)/\alpha_{set}$ with $\alpha_{set} = 100$ nm/s over 10 nm wavelength range.

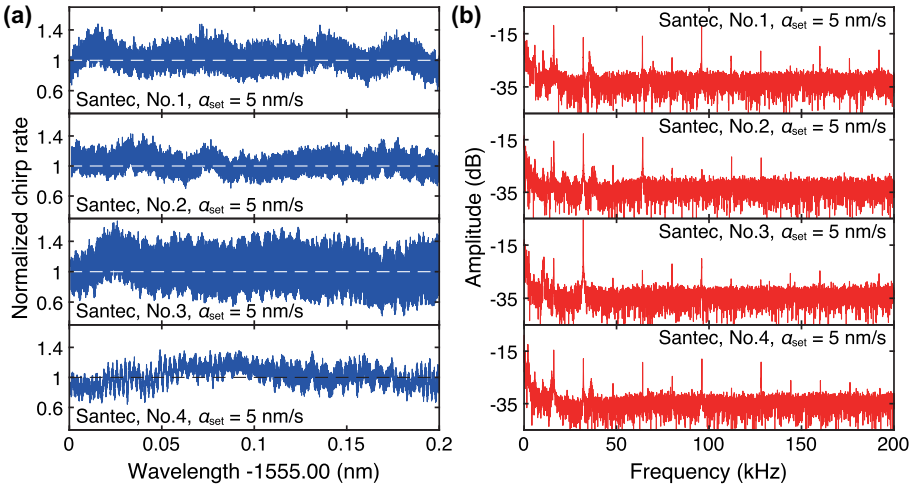

Fig. 7. Comparison of four Santec lasers' chirp dynamics in the wide tuning mode. (a) Normalized chirp rate $\alpha(\lambda)/\alpha_{set}$ of the four Santec lasers with $\alpha_{set} = 5$ nm/s over 0.2 nm wavelength range. (b) Frequency spectra of the chirp rate $\alpha(t)/\alpha_{set}$.

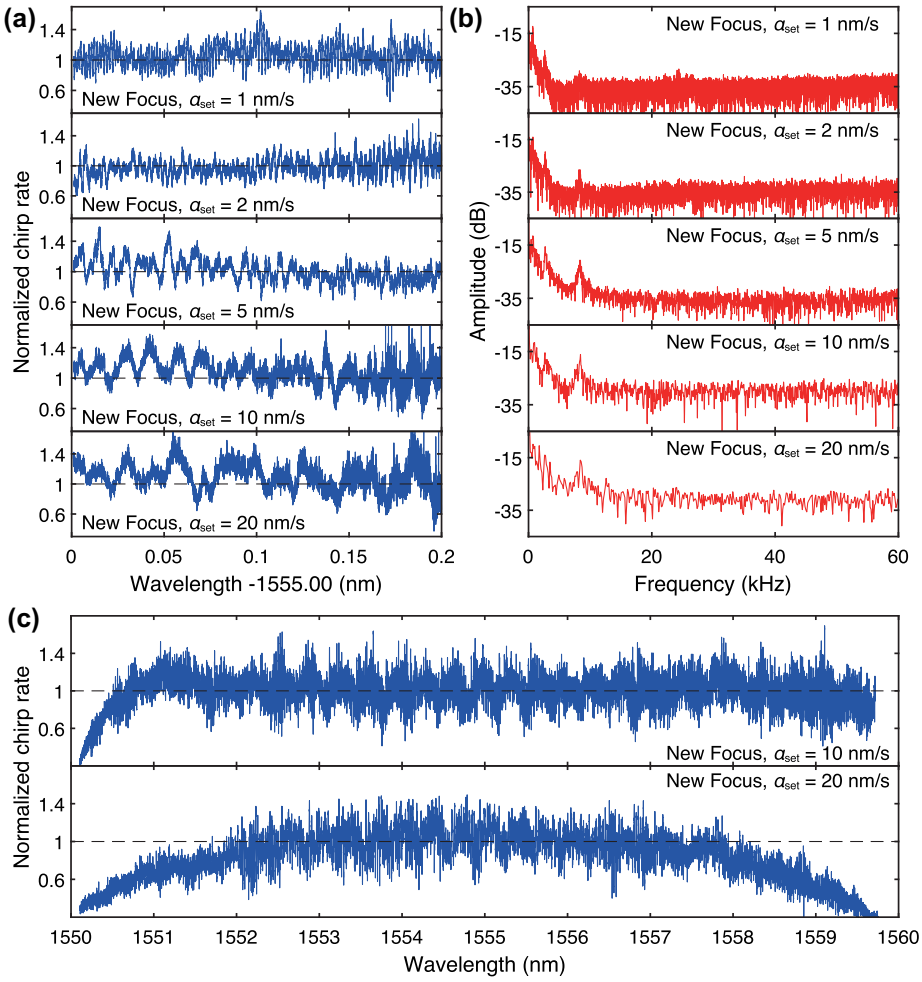

Fig. 8. Characterization of chirp dynamics of a New Focus laser in the wide tuning mode. (a) Normalized chirp rate $\alpha(\lambda)/\alpha_{set}$ with different set values α_{set} over 0.2 nm wavelength range. (b) Frequency spectra of the chirp rate $\alpha(t)/\alpha_{set}$. (c) Normalized chirp rate $\alpha(\lambda)/\alpha_{set}$ with different set values α_{set} over 10 nm wavelength range.

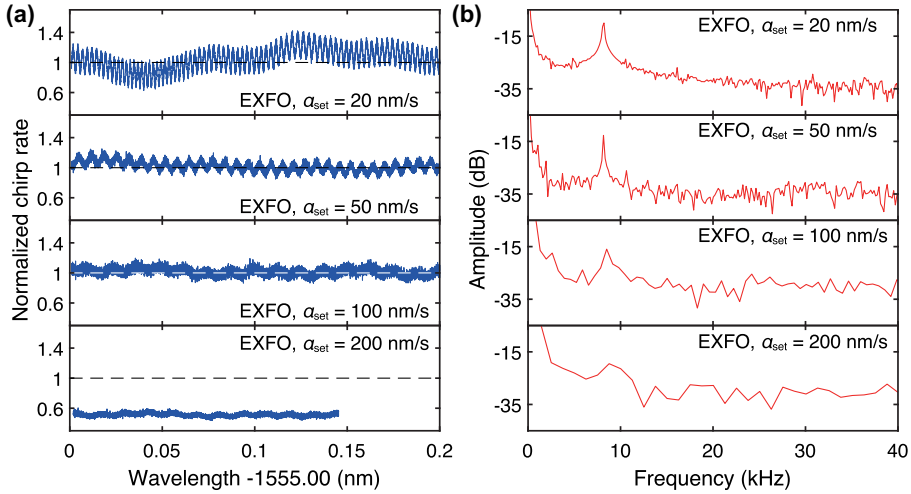

Fig. 9. Characterization of chirp dynamics of an EXFO laser in the wide tuning mode. (a) Normalized chirp rate $\alpha(\lambda)/\alpha_{set}$ with different set values α_{set} over 0.2 nm wavelength range. (b) Frequency spectra of the chirp rate $\alpha(t)/\alpha_{set}$.

after the first 5 nm chirp range (from 1550 to 1555 nm). After changing the chirp start wavelength from 1550 to 1540 nm, the laser can complete its acceleration before entering the test area and shows an RMSE of 5.1% and $\delta_L = 0.2\%$. Overall, the EXFO laser has optimal α_{set} of 100 nm/s.

APPENDIX B: LASER CHIRP DYNAMICS IN THE FINE TUNING MODE

The measurement includes three Toptica lasers, four Santec lasers, two New Focus lasers, and two NKT fiber lasers. The EXFO laser does not feature the fine tuning mode. These lasers are frequency-modulated at the central frequency of 193.3 THz and with an excursion range of 10 GHz (8 GHz for NKT lasers). The drive voltage signal to the piezo is either triangular or sinusoidal. Their modulation frequencies f_{mod} are set to 2, 10, 50, and 100 Hz. The traced chirp rate $\alpha(t)$ is converted to $\alpha(f_l)$ for a better comparison between cases with different α_{set}. A summary of different lasers' chirp dynamics with different f_{mod} is shown in Table 3.

The NKT lasers behave similarly with both triangular and sinusoidal drive signals, as shown in Fig. 10. The laser has significant jitter frequency of 25.09 kHz when $f_{mod} = 10$ Hz. This jitter frequency occurs in both NKT lasers, as shown in Fig. 11. However, the other main jitter frequency of 73.49 kHz only exists in one NKT laser. Jitter at these frequencies disappears at higher f_{mod}. Besides, Fig. 10(a) shows that, as f_{mod} increases, so does the chirp rate drift. Another manifestation of the NKT laser is that its actual chirp range does not reach the set value when f_{mod} is relatively high. The optimum f_{mod} for the NKT laser is 2 Hz, which actually works well at different modulation frequencies.

Like the NKT lasers, the Santec lasers also behave similarly with both triangular and sinusoidal drive signals. As shown in Fig. 12(a), the Santec laser's chirp rate drifts at all four tested f_{mod}. As f_{mod} increases, the actual chirp range of the Santec laser decreases. In the frequency domain, the laser has significant jitter frequencies of 0.66 and 1.89 kHz at $f_{mod} = 2$ Hz, and these jitters disappear at higher f_{mod}, as shown in Fig. 12(b). Comparing the chirp dynamics of four Santec lasers at $f_{mod} = 2$ Hz, as shown in Fig. 13, it is found that all four Santec lasers exhibit a jitter frequency of 0.66 kHz. However, the 1.89 kHz jitter frequency occurs only in two of them. Overall, Santec lasers work best when driven by a 10 Hz triangular wave.

The results for the Toptica lasers are shown in Fig. 14. For the triangular drive signal of 50 and 100 Hz, an obvious chirp rate jitter can be observed. Meanwhile for the situation when a sinusoidal signal is input, the jitter is not evident. In the frequency domain, as shown in Fig. 14(b), the jitter frequency can be directly obtained as 3.84 kHz, which is likely the resonant frequency of the fundamental mechanical mode excited by high-order components of the high f_{mod} triangular input signal. To make this easier to understand, three different drive signals are shown in Fig. 15(a), and their Fourier transforms

Table 3. Comparison of Laser Chirp Dynamics of Different Lasers in the Fine Tuning Mode

Laser Brand	Model	Tuning Mode	f_{mod}	Chirp Range	RMSE	δ_L
Toptica	CTL 1550	Piezo, triangular	2 Hz	10 GHz	8.9% (2.1%)	0.8% (0.0%)
Toptica	CTL 1550	Piezo, sinusoidal	2 Hz	10 GHz	8.0% (0.4%)	–
Toptica	CTL 1550	Piezo, triangular	10 Hz	10 GHz	7.8% (1.3%)	0.8% (0.0%)
Toptica	CTL 1550	Piezo, sinusoidal	10 Hz	10 GHz	7.5% (0.1%)	–
Toptica	CTL 1550	Piezo, triangular	50 Hz	10 GHz	10.1% (1.3%)	0.9% (0.0%)
Toptica	CTL 1550	Piezo, sinusoidal	50 Hz	10 GHz	7.4% (0.2%)	–
Toptica	CTL 1550	Piezo, triangular	100 Hz	10 GHz	15.6% (3.5%)	0.9% (0.0%)
Toptica	CTL 1550	Piezo, sinusoidal	100 Hz	10 GHz	11.8% (0.2%)	–
Santec	TSL-570-A	Piezo, triangular	2 Hz	10 GHz	18.5% (2.8%)	1.8% (0.1%)
Santec	TSL-570-A	Piezo, sinusoidal	2 Hz	10 GHz	18.8% (6.0%)	–
Santec	TSL-570-A	Piezo, triangular	10 Hz	10 GHz	14.1% (0.6%)	1.8% (0.1%)
Santec	TSL-570-A	Piezo, sinusoidal	10 Hz	10 GHz	16.4% (0.5%)	–
Santec	TSL-570-A	Piezo, triangular	50 Hz	10 GHz	23.8% (0.7%)	2.8% (0.1%)
Santec	TSL-570-A	Piezo, sinusoidal	50 Hz	10 GHz	25.9% (0.5%)	–
Santec	TSL-570-A	Piezo, triangular	100 Hz	10 GHz	44.4% (1.1%)	3.3% (0.3%)
Santec	TSL-570-A	Piezo, sinusoidal	100 Hz	10 GHz	45.3% (1.0%)	–
New Focus	TLB-6700	Piezo, triangular	50 Hz	10 GHz	17.9% (12.1%)	0.4% (0.1%)
New Focus	TLB-6700	Piezo, sinusoidal	50 Hz	10 GHz	11.9% (9.3%)	–
New Focus	TLB-6700	Piezo, triangular	100 Hz	10 GHz	34.5% (5.5%)	1.3% (0.1%)
New Focus	TLB-6700	Piezo, sinusoidal	100 Hz	10 GHz	8.4% (4.2%)	–
NKT	E15	Piezo, triangular	2 Hz	8 GHz	5.6% (1.9%)	0.5% (0.3%)
NKT	E15	Piezo, sinusoidal	2 Hz	8 GHz	6.5% (1.0%)	–
NKT	E15	Piezo, triangular	10 Hz	8 GHz	5.8% (1.5%)	0.6% (0.3%)
NKT	E15	Piezo, sinusoidal	10 Hz	8 GHz	7.5% (1.9%)	–
NKT	E15	Piezo, triangular	50 Hz	8 GHz	11.3% (3.1%)	1.2% (0.5%)
NKT	E15	Piezo, sinusoidal	50 Hz	8 GHz	17.8% (2.9%)	–
NKT	E15	Piezo, triangular	100 Hz	8 GHz	18.5% (3.4%)	2.2% (0.5%)
NKT	E15	Piezo, sinusoidal	100 Hz	8 GHz	34.6% (4.1%)	–

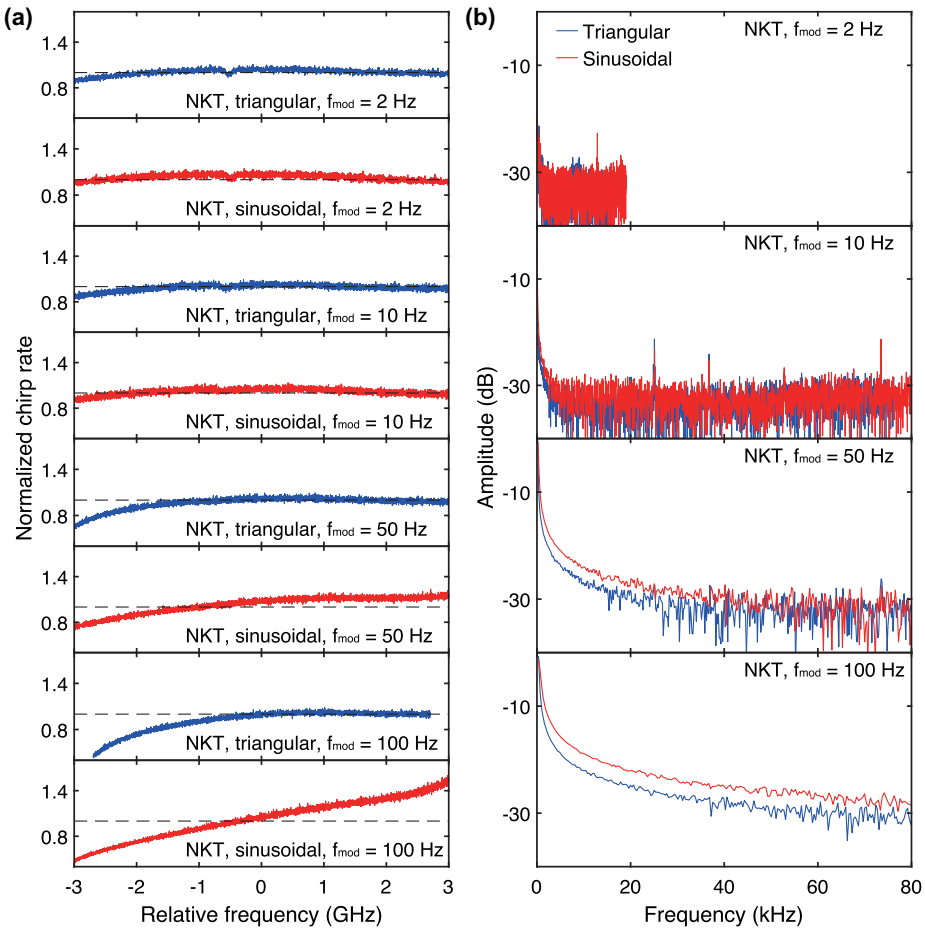

Fig. 10. Characterization of chirp dynamics of an NKT laser in the fine tuning mode. (a) Normalized chirp rate $\alpha(f_l)/\alpha_{\text{set}}$ with different set values f_{mod} over 6 GHz frequency range. The piezo of the laser is driven by a triangular (blue) or a sinusoidal (red) signal. (b) Frequency spectra of the chirp rate $\alpha(t)/\alpha_{\text{set}}$.

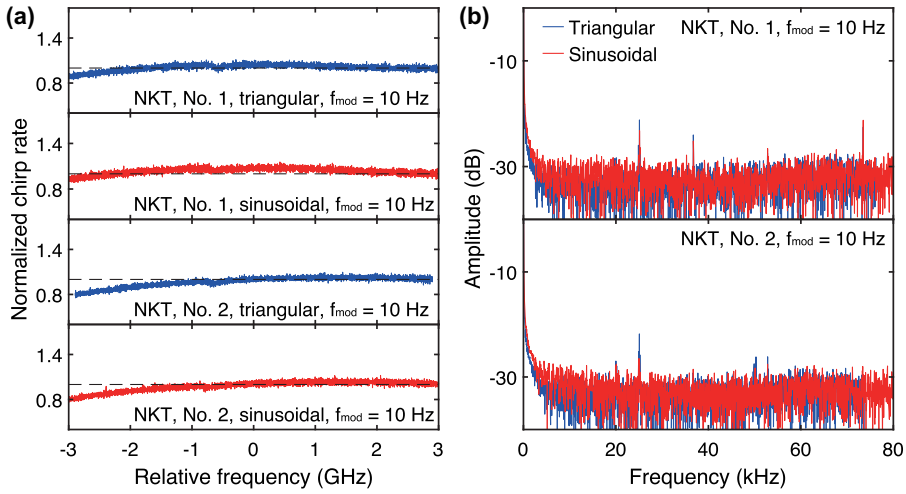

Fig. 11. Characterization of chirp dynamics of two NKT lasers in the fine tuning mode. (a) Normalized chirp rate $\alpha(f_l)/\alpha_{\text{set}}$ with $f_{\text{mod}} = 10$ Hz over 6 GHz frequency range. The piezo of the laser is driven by a triangular (blue) or a sinusoidal (red) signal. (b) Frequency spectra of the chirp rate $\alpha(t)/\alpha_{\text{set}}$.

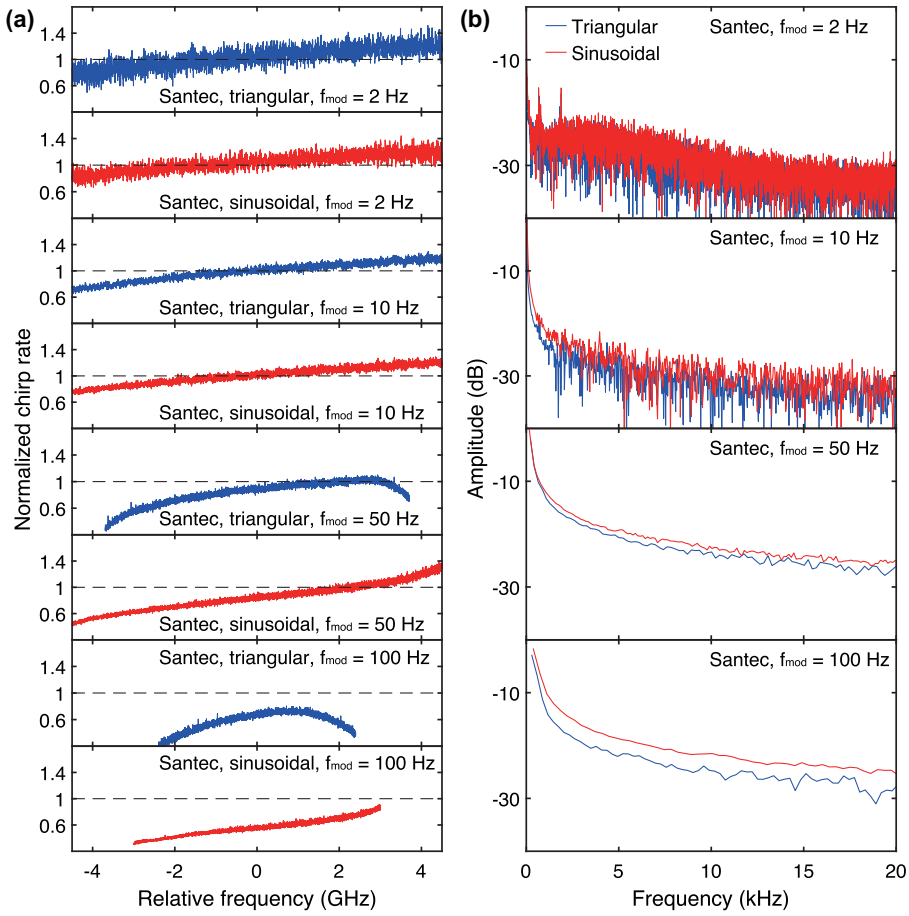

Fig. 12. Characterization of chirp dynamics of a Santec laser in the fine tuning mode. (a) Normalized chirp rate $\alpha(f_l)/\alpha_{\text{set}}$ with different set values f_{mod} over 9 GHz frequency range. The piezo of the laser is driven by a triangular (blue) or a sinusoidal (red) signal. (b) Frequency spectra of the chirp rate $\alpha(t)/\alpha_{\text{set}}$.

are shown in Fig. 15(b). It can be seen that triangular waves contain many high-frequency components. The higher the drive frequency, the higher the amplitude around the 3.84 kHz frequency of the triangular waveform. Thus, the triangular wave drive signal tends to excite the resonance of the laser cavity. This manifestation occurs in all three Toptica lasers, as shown in Fig. 16, proven to be the feature of the Toptica lasers. Besides, as shown in Fig. 14(b), at a modulation frequency of $f_{\text{mod}} = 10$ Hz, higher-order mechanical modes with frequencies of 28.24 and 56.45 kHz can also be observed. As the chirp rate increases, these obvious high-frequency resonances disappear. Overall, Toptica lasers should be driven sinusoidally, and their optimum modulation frequency is 50 Hz.

The New Focus lasers exhibit mode hopping when f_{mod} equals 10 or 20 Hz, so the corresponding chirp dynamics characterizations are not shown. As shown in Fig. 17, like Toptica lasers, the New Focus laser's fundamental mechanical mode of 1.10 kHz can be excited by a triangular-driven signal. Thus, the New Focus lasers should be modulated by sinusoidal signals, and their optimum f_{mod} is 100 Hz.

APPENDIX C: LASER TUNING DYNAMICS CHARACTERIZATION FOR LIDAR DEMONSTRATION

In FMCW LiDAR, the fine tuning mode is commonly used because of its low duty cycle. Here we chose a Toptica laser for the LiDAR demonstration because it has the largest chirp range, 35 GHz, out of our four types of lasers. We make the laser chirp around the central frequency of 193.3 THz and the chirp range of 35 GHz. Some typical laser chirp dynamics characterizations are shown in Fig. 18. Still, we can observe the fundamental mode of 3.84 kHz excited by 50 Hz triangular-driven signal. Besides, higher-order mechanical modes can also be observed from the upper panel of Fig. 18(b), i.e., with a frequency of 56.43 kHz. As f_{mod} increases, the noise floor of the frequency-domain chirp rate increases, but the obvious high-frequency resonances disappear, as shown in the lower panel of Fig. 18(b).

Next, we characterized the effect of our pre-linearization method. We first measured the laser's chirp rate three times. The averaged result is used as the pre-linearization chirp rate $\alpha_c(t)$, as shown in the upper panel of Fig. 18(c).

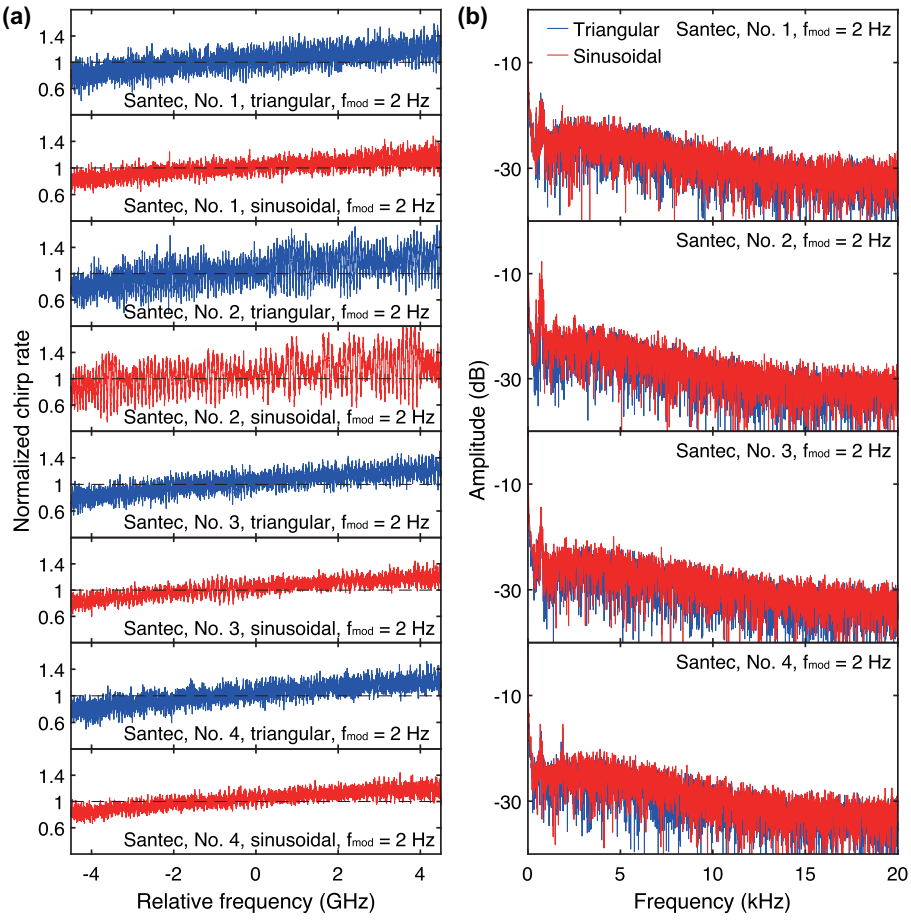

Fig. 13. Characterization of chirp dynamics of four Santec lasers in the fine tuning mode. (a) Normalized chirp rate $\alpha(f_l)/\alpha_{\text{set}}$ with $f_{\text{mod}} = 2$ Hz over 9 GHz frequency range. The piezo of the laser is driven by a triangular (blue) or a sinusoidal (red) signal. (b) Frequency spectra of the chirp rate $\alpha(t)/\alpha_{\text{set}}$.

The pre-obtained $\alpha_c(t)$ is used to perform chirp rate linearization. To verify the effectiveness of linearization, we characterized the laser again as the real-time measurement $\alpha(t)$. Their consistency is compared by $\alpha(t)/\alpha_c(t)$ as shown in the lower panel of Fig. 18(c). Clearly, the chirp rate drift is eliminated. Its Fourier transform spectrum is shown in Fig. 18(d). The average oscillation (calculated by averaging the amplitude of the frequency spectrum below 100 kHz) is shown by a dotted and dashed line. Compared with the average oscillation of $\alpha(t)/\alpha_{\text{set}}(t)$'s frequency spectrum, shown by the dashed line, the oscillation level has been attenuated by 7.4 dB. However, jitter frequencies of 3.84 and 56.43 kHz still exist, indicating the random nature of the chirp rate jitter generated by the cavity resonances. This fact implies that the avoidance of cavity resonance is crucial to reducing the phase noise of a pre-linearized tunable laser. Thus, in our case, a 50-Hz sinusoidal drive signal is utilized for LiDAR demonstration.

APPENDIX D: SETUP FOR LIDAR DEMONSTRATION AND PRECISION TEST

With the pre-obtained $\alpha_c(t)$, the LiDAR demonstration can proceed without any extra linearization unit. As shown in Fig. 19(a), the frequency-modulated laser is split into two paths. In one path, the laser passes through a collimator, enters free space, is reflected by the target, and is recollected. The reflected laser is then combined with the reference path, and the beat signal between the two paths is recorded by a balanced photodetector.

To test the long-term stability of pre-linearization, a fixed mirror is used as the target at a distance of 53.361 mm and measured 1128 times every 3 s. Their relative distance histogram is shown in Fig. 19(b) with a standard deviation of 11 μm, showing the long-term stability of our pre-linearization method.

APPENDIX E: COMPARISON WITH THE FREQUENCY-CALIBRATION METHOD USING AN UNBALANCED MACH–ZEHNDER INTERFEROMETER

Here we compare our frequency-comb-calibration method with the one using a UMZI. References [15–17] linearize the tunable laser with the UMZI for OFDR application. References [21,22] use the frequency-comb-calibrated UMZI for wideband laser linearization. However, in these works,

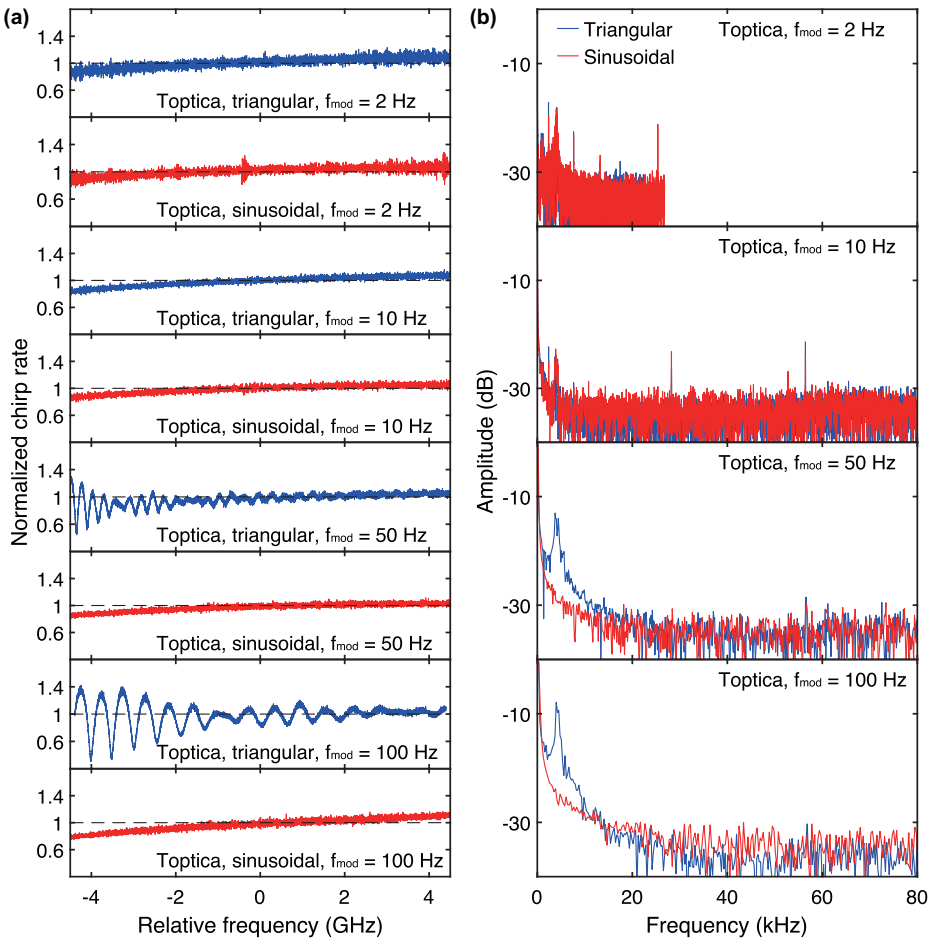

Fig. 14. Characterization of chirp dynamics of a Toptica laser in the fine tuning mode. (a) Normalized chirp rate $\alpha(f_l)/\alpha_{\text{set}}$ with different set values f_{mod} over 9 GHz frequency range. The piezo of the laser is driven by a triangular (blue) or a sinusoidal (red) signal. (b) Frequency spectra of the chirp rate $\alpha(t)/\alpha_{\text{set}}$.

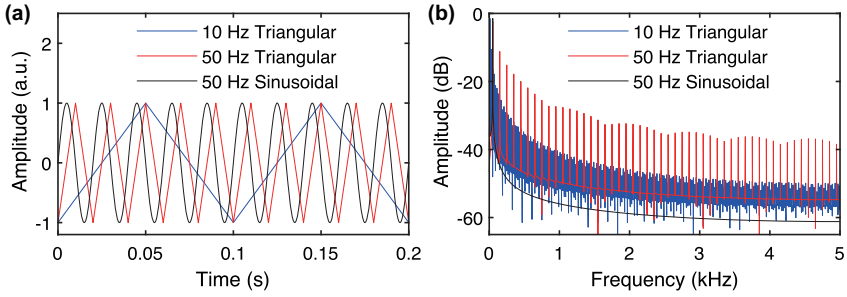

Fig. 15. (a) Different drive signals. (b) Fourier transform of different drive signals.

the method using UMZI is valid only if the laser is mode-hop-free and with uni-directional chirping. Commonly a small FSR of the UMZI, e.g., 5 MHz, is used experimentally. Therefore, if the laser frequency hops by $\Delta f = N \times \text{FSR} + \delta$ ($|\delta| < \text{FSR}$; N is an integer), one cannot correctly count N. Meanwhile, it is also challenging to judge whether the laser chirps backward, i.e., $\Delta f < 0$. Therefore, frequency calibration using a UMZI is valid only if the tunable laser is mode-hop-free and has uni-directional chirping. In comparison, our method using 95 digital band-pass filters (separated by 1 MHz) and a self-referenced optical frequency comb is not nullified by this issue. In fact, our method can examine

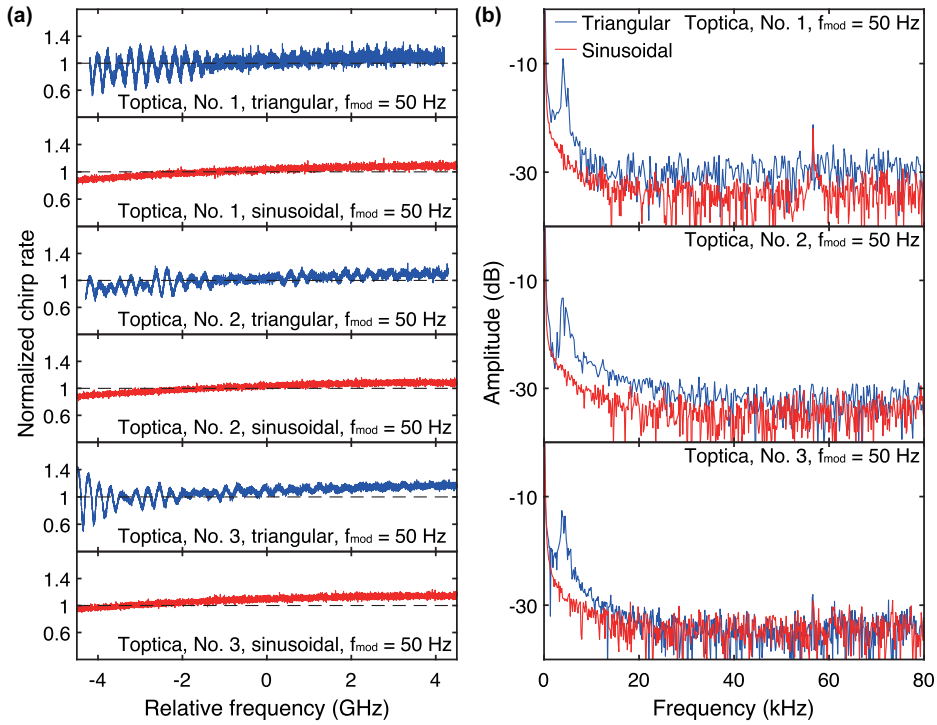

Fig. 16. Characterization of chirp dynamics of three Toptica lasers in the fine tuning mode. (a) Normalized chirp rate $\alpha(f_l)/\alpha_{\text{set}}$ with $f_{\text{mod}} = 50$ Hz over 9 GHz frequency range. The piezo of the laser is driven by a triangular (blue) or a sinusoidal (red) signal. (b) Frequency spectra of the chirp rate $\alpha(t)/\alpha_{\text{set}}$.

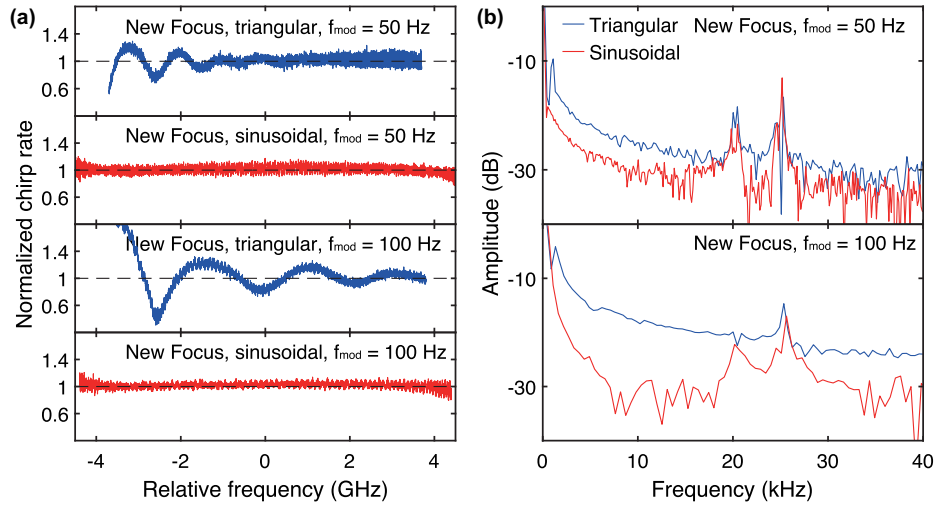

Fig. 17. Characterization of chirp dynamics of a New Focus laser in the fine tuning mode. (a) Normalized chirp rate $\alpha(f_l)/\alpha_{\text{set}}$ with different set values f_{mod} over 9 GHz frequency range. The piezo of the laser is driven by a triangular (blue) or a sinusoidal (red) signal. (b) Frequency spectra of the chirp rate $\alpha(t)/\alpha_{\text{set}}$.

whether the tunable laser is indeed mode-hop-free and has unidirectional chirping, which validates the previous method with a UMZI.

In addition, the frequency calibration method using a UMZI suffers from the following issues.

(i) The delay time τ between the UMZI's two arms cannot be measured accurately and precisely.

(ii) Due to fiber dispersion, τ varies with laser frequency/wavelength; thus the precision of a fiber UMZI is compromised further with a wider laser chirp range (up to tens of nanometers).

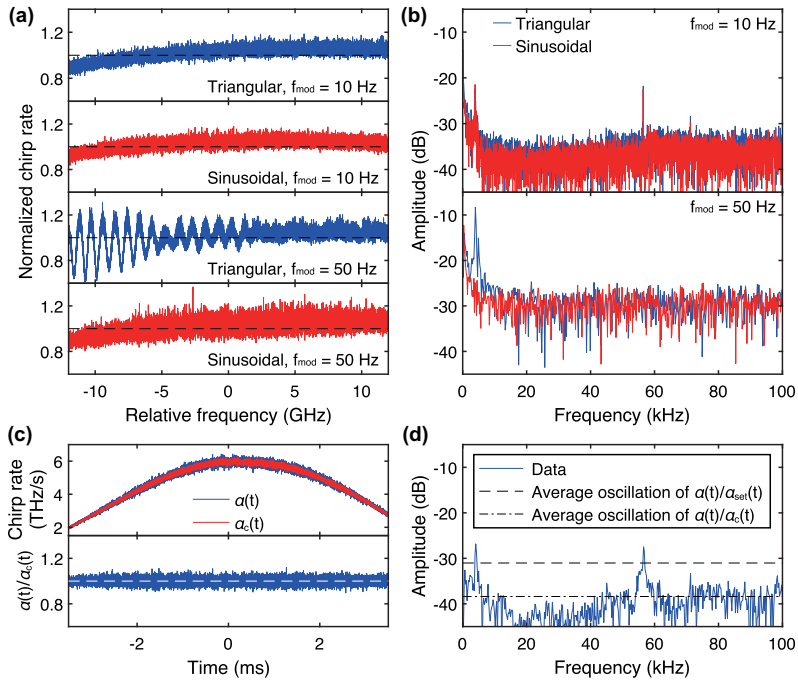

Fig. 18. Laser characterization for LiDAR demonstration. (a) Normalized chirp rate $\alpha(f_l)/\alpha_{\text{set}}$ with different set values f_{mod} over 24 GHz frequency range. The piezo of the laser is driven by a triangular (blue) or a sinusoidal (red) signal. (b) Frequency spectra of the chirp rate $\alpha(t)/\alpha_{\text{set}}$. (c) Upper panel shows the chirp rate curve $\alpha(t)$ (blue) and pre-linearization curve $\alpha_c(t)$ (red). Lower panel shows the linearized chirp rate curve $\alpha(t)/\alpha_c(t)$. (d) Frequency spectrum of the linearized chirp rate in the lower panel of panel (c). The dotted and dashed line shows its averaged amplitude below 100 kHz. The dashed line shows the averaged amplitude of normalized chirp rate $\alpha(t)/\alpha_{\text{set}}(t)$'s frequency spectrum below 100 kHz.

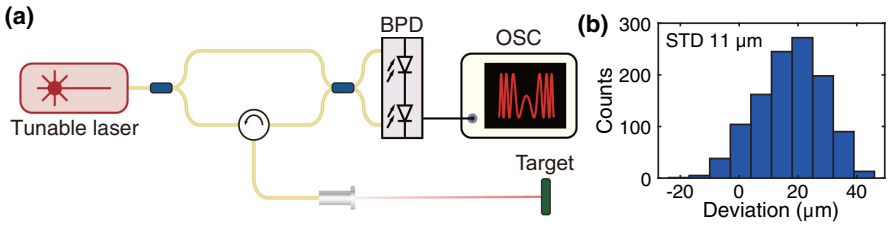

Fig. 19. Setup for LiDAR demonstration and precision test. (a) Experimental setup. BPD, balanced photodetector; OSC, oscilloscope. (b) Histogram of deviation of ranging measurement. The long-term stability of pre-linearization is verified by a precision test. A mirror is fixed at a distance of 53.361 mm and measured 1128 times every 3 s. The standard deviation of the measured distance is 11 μm.

(iii) The UMZI's performance is subjected to environmental perturbations. Minuscule vibration or temperature fluctuation can change the delay time of the UMZI and result in frequency calibration errors.

Further frequency referencing using an optical frequency comb can solve the abovementioned issue (ii) of the UMZI, but not (i) and (iii). While our method uses a frequency comb but no UMZI, we do not suffer from the issues (i)–(iii).

Funding. China Postdoctoral Science Foundation (2022M721482); Guangdong Provincial Key Laboratory (2019B121203002); Shenzhen-Hong Kong Cooperation Zone for Technology and Innovation (HZQB-KCZYB2020050); National Natural Science Foundation of China (12261131503).

Acknowledgment. We thank EXFO for lending us one laser for characterization. J. Liu acknowledges support from the NSFC, Shenzhen-Hong Kong Cooperation Zone for Technology and Innovation, and Guangdong Provincial Key Laboratory. Y.-H L. acknowledges support from the China Postdoctoral Science Foundation.

B. S., W. S., Y.-H. L., and J. Long built the experimental setup, with assistance from X. B. and A. W. B. S. performed the laser characterization. B. S. and Y. H., and Y.-H. L. performed the LiDAR experiments. B. S., W. S., Y.-H. L., and J. Liu

analyzed the data and prepared the manuscript with input from others. J. Liu supervised the project.

Disclosures. B. S., Y.-H. L., W. S., X. B., and J. Liu filed a patent application for the tunable laser characterization and linearization method. Others declare no conflicts of interest.

Data Availability. The code and data used to produce the plots within this work are available on Zenodo [53]. All other data used in this study are available from the corresponding authors upon reasonable request.

REFERENCES

1. B. Cense, N. A. Nassif, T. C. Chen, *et al.*, "Ultrahigh-resolution high-speed retinal imaging using spectral-domain optical coherence tomography," Opt. Express **12**, 2435–2447 (2004).
2. I. Grulkowski, J. J. Liu, B. Potsaid, *et al.*, "Retinal, anterior segment and full eye imaging using ultrahigh speed swept source OCT with vertical-cavity surface emitting lasers," Biomed. Opt. Express **3**, 2733–2751 (2012).
3. H. J. Shammas, S. Ortiz, M. C. Shammas, *et al.*, "Biometry measurements using a new large-coherence-length swept-source optical coherence tomographer," J. Cataract Refract. Surg. **42**, 50–61 (2016).
4. F. Lexer, C. K. Hitzenberger, A. F. Fercher, *et al.*, "Wavelength-tuning interferometry of intraocular distances," Appl. Opt. **36**, 6548–6553 (1997).
5. B. J. Soller, D. K. Gifford, M. S. Wolfe, *et al.*, "High resolution optical frequency domain reflectometry for characterization of components and assemblies," Opt. Express **13**, 666–674 (2005).
6. J. Liu, V. Brasch, M. H. P. Pfeiffer, *et al.*, "Frequency-comb-assisted broadband precision spectroscopy with cascaded diode lasers," Opt. Lett. **41**, 3134–3137 (2016).
7. R. Gotti, T. Puppe, Y. Mayzlin, *et al.*, "Comb-locked frequency-swept synthesizer for high precision broadband spectroscopy," Sci. Rep. **10**, 2523 (2020).
8. X. Liu and Y. Ma, "Tunable diode laser absorption spectroscopy based temperature measurement with a single diode laser near 1.4 μm," Sensors **22**, 2733–2751 (2022).
9. P. A. Roos, R. R. Reibel, T. Berg, *et al.*, "Ultrabroadband optical chirp linearization for precision metrology applications," Opt. Lett. **34**, 3692–3694 (2009).
10. E. Baumann, F. R. Giorgetta, I. Coddington, *et al.*, "Comb-calibrated frequency-modulated continuous-wave ladar for absolute distance measurements," Opt. Lett. **38**, 2026–2028 (2013).
11. N. Kuse and M. E. Fermann, "Frequency-modulated comb lidar," APL Photonics **4**, 106105 (2019).
12. M. Okano and C. Chong, "Swept source lidar: simultaneous FMCW ranging and nonmechanical beam steering with a wideband swept source," Opt. Express **28**, 23898–23915 (2020).
13. I. Kim, R. J. Martins, J. Jang, *et al.*, "Nanophotonics for light detection and ranging technology," Nat. Nanotechnol. **16**, 508–524 (2021).
14. G. Lihachev, J. Riemensberger, W. Weng, *et al.*, "Low-noise frequency-agile photonic integrated lasers for coherent ranging," Nat. Commun. **13**, 3522 (2022).
15. U. Glombitza and E. Brinkmeyer, "Coherent frequency-domain reflectometry for characterization of single-mode integrated-optical waveguides," J. Lightwave Technol. **11**, 1377–1384 (1993).
16. T. Ahn, J. Y. Lee, and D. Y. Kim, "Suppression of nonlinear frequency sweep in an optical frequency-domain reflectometer by use of Hilbert transformation," Appl. Opt. **44**, 7630–7634 (2005).
17. M. Badar, P. Lu, M. Buric, *et al.*, "Integrated auxiliary interferometer for self-correction of nonlinear tuning in optical frequency domain reflectometry," J. Lightwave Technol. **38**, 6097–6103 (2020).
18. X. Zhang, J. Pouls, and M. C. Wu, "Laser frequency sweep linearization by iterative learning pre-distortion for FMCW lidar," Opt. Express **27**, 9965–9974 (2019).
19. P. Del'Haye, O. Arcizet, M. L. Gorodetsky, *et al.*, "Frequency comb assisted diode laser spectroscopy for measurement of microcavity dispersion," Nat. Photonics **3**, 529–533 (2009).
20. F. R. Giorgetta, I. Coddington, E. Baumann, *et al.*, "Fast high-resolution spectroscopy of dynamic continuous-wave laser sources," Nat. Photonics **4**, 853–857 (2010).
21. S. Fujii and T. Tanabe, "Dispersion engineering and measurement of whispering gallery mode microresonator for Kerr frequency comb generation," Nanophotonics **9**, 1087–1104 (2020).
22. K. Twayana, Z. Ye, Ó. B. Helgason, *et al.*, "Frequency-comb-calibrated swept-wavelength interferometry," Opt. Express **29**, 24363–24372 (2021).
23. T. Udem, R. Holzwarth, and T. W. Hänsch, "Optical frequency metrology," Nature **416**, 233–237 (2002).
24. S. T. Cundiff and J. Ye, "Colloquium: femtosecond optical frequency combs," Rev. Mod. Phys. **75**, 325–342 (2003).
25. S. A. Diddams, K. Vahala, and T. Udem, "Optical frequency combs: coherently uniting the electromagnetic spectrum," Science **369**, eaay3676 (2020).
26. L. Marple, "Computing the discrete-time "analytic" signal via FFT," IEEE Trans. Signal Process. **47**, 2600–2603 (1999).
27. T. Herr, V. Brasch, J. D. Jost, *et al.*, "Temporal solitons in optical microresonators," Nat. Photonics **8**, 145–152 (2013).
28. H. Guo, M. Karpov, E. Lucas, *et al.*, "Universal dynamics and deterministic switching of dissipative Kerr solitons in optical microresonators," Nat. Phys. **13**, 94–102 (2017).
29. P. Trocha, M. Karpov, D. Ganin, *et al.*, "Ultrafast optical ranging using microresonator soliton frequency combs," Science **359**, 887–891 (2018).
30. M.-G. Suh and K. J. Vahala, "Soliton microcomb range measurement," Science **359**, 884–887 (2018).
31. H. Zhou, Y. Geng, W. Cui, *et al.*, "Soliton bursts and deterministic dissipative Kerr soliton generation in auxiliary-assisted microcavities," Light Sci. Appl. **8**, 50 (2019).
32. J. Liu, E. Lucas, A. S. Raja, *et al.*, "Photonic microwave generation in the X- and K-band using integrated soliton microcombs," Nat. Photonics **14**, 486–491 (2020).
33. H. Weng, J. Liu, A. A. Afridi, *et al.*, "Directly accessing octave-spanning dissipative Kerr soliton frequency combs in an AlN microresonator," Photonics Res. **9**, 1351–1357 (2021).
34. D. Xia, Z. Yang, P. Zeng, *et al.*, "Integrated chalcogenide photonics for microresonator soliton combs," Laser Photonics Rev. **17**, 2200219 (2023).
35. K. Liu, Z. Wang, S. Yao, *et al.*, "Mitigating fast thermal instability by engineered laser sweep in AlN soliton microcomb generation," Photonics Res. **11**, A10–A18 (2023).
36. Y. Bai, M. Zhang, Q. Shi, *et al.*, "Brillouin-Kerr soliton frequency combs in an optical microresonator," Phys. Rev. Lett. **126**, 063901 (2021).
37. Y.-H. Luo, B. Shi, W. Sun, *et al.*, "A wideband, high-resolution vector spectrum analyzer for integrated photonics," arXiv, arXiv:2304.04295 (2023).
38. C. L. Giusca, R. K. Leach, and F. Helery, "Calibration of the scales of areal surface topography measuring instruments: part 2. amplification, linearity and squareness," Meas. Sci. Technol. **23**, 065005 (2012).
39. M. A. Lefsky, W. B. Cohen, G. G. Parker, *et al.*, "Lidar remote sensing for ecosystem studies," Bioscience **52**, 19–30 (2002).
40. M. P. Simard, N. F. Pinto, B. Joshua, *et al.*, "Mapping forest canopy height globally with spaceborne lidar," J. Geophys. Res. Biogeosci. **116**, G04021 (2011).
41. F. G. Fernald, "Analysis of atmospheric lidar observations: some comments," Appl. Opt. **23**, 652–653 (1984).
42. M. A. Vaughan, K. A. Powell, D. M. Winker, *et al.*, "Fully automated detection of cloud and aerosol layers in the calipso lidar measurements," J. Atmos. Ocean. Technol. **26**, 2034–2050 (2009).

43. D. J. Mulla, "Twenty five years of remote sensing in precision agriculture: key advances and remaining knowledge gaps," Biosyst. Eng. **114**, 358–371 (2013).
44. X. Chen, H. Ma, J. Wan, *et al.*, "Multi-view 3D object detection network for autonomous driving," in *IEEE Conference on Computer Vision and Pattern Recognition (CVPR)* (2017), pp. 6526–6534.
45. X. Yue, B. Wu, S. A. Seshia, *et al.*, "A lidar point cloud generator: from a virtual world to autonomous driving," in *Proceedings of the 2018 ACM on International Conference on Multimedia Retrieval* (2018), pp. 458–464.
46. A. Lukashchuk, J. Riemensberger, A. Stroganov, *et al.*, "Chaotic microcomb inertia-free parallel ranging," APL Photonics **8**, 056102 (2023).
47. R. Chen, H. Shu, B. Shen, *et al.*, "Breaking the temporal and frequency congestion of lidar by parallel chaos," Nat. Photonics **17**, 306–314 (2023).
48. A. F. Chase, D. Z. Chase, J. F. Weishampel, *et al.*, "Airborne lidar, archaeology, and the ancient Maya landscape at Caracol, Belize," J. Archaeolog. Sci. **38**, 387–398 (2011).
49. A. F. Chase, D. Z. Chase, C. T. Fisher, *et al.*, "Geospatial revolution and remote sensing lidar in mesoamerican archaeology," Proc. Natl. Acad. Sci. USA **109**, 12916–12921 (2012).
50. D. H. Evans, R. J. Fletcher, C. Pottier, *et al.*, "Uncovering archaeological landscapes at angkor using lidar," Proc. Natl. Acad. Sci. USA **110**, 12595–12600 (2013).
51. M.-C. Amann, T. M. Bosch, M. Lescure, *et al.*, "Laser ranging: a critical review of unusual techniques for distance measurement," Opt. Eng. **40**, 10–19 (2001).
52. K. A. Shinpaugh, R. L. Simpson, A. L. Wicks, *et al.*, "Signal-processing techniques for low signal-to-noise ratio laser Doppler velocimetry signals," Exp. Fluids **12**, 319–328 (1992).
53. Zenodo, https://doi.org/10.5281/zenodo.10602748.

S 183.146.49 (By 2024-07-30 21:27:15)